PHYSICAL REVIEW E **91**, 030301(R) (2015)

Crystallization and reentrant melting of charged colloids in nonpolar solvents

Toshimitsu Kanai,[1] Niels Boon,[2] Peter J. Lu (陸述義),[1,*] Eli Sloutskin,[1] Andrew B. Schofield,[3] Frank Smallenburg,[4]
René van Roij,[2] Marjolein Dijkstra,[4] and David A. Weitz[1]
[1]*Department of Physics and SEAS, Harvard University, Cambridge, Massachusetts 02138, USA*
[2]*Institute for Theoretical Physics, Utrecht University, Leuvenlaan 4, 3584 CE Utrecht, The Netherlands*
[3]*The School of Physics, University of Edinburgh, Edinburgh EH9 3FD, United Kingdom*
[4]*Soft Condensed Matter, Debye Institute for Nanomaterials Science, Utrecht University, Princetonplein 5, 3584 CC Utrecht, The Netherlands*

(Received 8 August 2014; published 23 March 2015)

We explore the crystallization of charged colloidal particles in a nonpolar solvent mixture. We simultaneously charge the particles and add counterions to the solution with aerosol-OT (AOT) reverse micelles. At low AOT concentrations, the charged particles crystallize into body-centered-cubic (bcc) or face-centered-cubic (fcc) Wigner crystals; at high AOT concentrations, the increased screening drives a thus far unobserved reentrant melting transition. We observe an unexpected scaling of the data with particle size, and account for all behavior with a model that quantitatively predicts both the reentrant melting and the data collapse.

DOI: 10.1103/PhysRevE.91.030301 PACS number(s): 82.70.Dd, 61.50.Ks, 64.60.Cn, 64.70.pv

Colloidal particles can spontaneously form structures that exhibit long-range ordered states, making them a fascinating system for fundamental studies of crystal phase behavior [1–4]. The majority of studies focus on colloids which model the hard-sphere interaction, a strong repulsion that prevents particles from overlapping, whose range is restricted to contact [5]. Hard-sphere crystallization is driven through purely entropic effects, and the phase behavior is well studied [5–9]. Typically, the colloids used for these studies are sterically-stabilized polymeric particles in nonaqueous solvents, which can match both the density ρ and refractive index n of the particles, enabling confocal microscopy to be used for these investigations. Even earlier studies focused on charged particles, where crystallization is driven by strong long-range repulsive interactions arising from Coulombic charges on the particles [1,10–22]. These studies were performed on particles in aqueous solvents, which makes charge effects much easier to induce, but precludes index matching, limiting the use of optical techniques except at very low densities. Instead, x-ray scattering studies [23] showed a fascinating phase behavior of Wigner crystals, including a body-centered-cubic (bcc) phase at low concentration, and a solid-solid transition to a face-centered-cubic (fcc) phase at higher densities [15–18,24,25]. It is also possible to induce charge on particles in nonaqueous solvents through the addition of charge control agents [21,26–28]. However, in this case, there is strong coupling between the charge on the particle surface and the ions in solution. Charge-induced crystallization should still be expected, although new behavior may also occur as a consequence of this coupling. Nevertheless, these systems have never been investigated experimentally, and the range of potential behavior has not yet been explored.

In this Rapid Communication, we investigate the crystallization behavior of colloidal particles in nonpolar solvents. By adding aerosol-OT (AOT) reverse micelles, we both charge the particles and add ions to the solution. As AOT concentration increases from zero, the system undergoes a first transition from fluid to a charge-stabilized bcc Wigner crystal, and then a second solid-solid transition from bcc to fcc. Further increasing reverse-micelle concentration leads to a surprising behavior: highly charged particles undergo a reentrant transition from fcc crystal back to a fluid; the reverse micelles screen the charge they induce, destroying the Wigner crystals. We observe the same behavior for several different particle sizes and over a wide range of particle volume fractions ϕ below the hard-sphere crystallization boundary. Strikingly, we observe the phase boundaries to collapse onto a single master curve only when the particle size is included explicitly, in contrast to findings in all other systems. To explain these observations, we present a model for the charging effects of the reverse micelles, and solve the Poisson-Boltzmann equation in a spherical shell to determine the potential and background charge density. Numerical solutions and a mapping onto the one-component plasma model predict the full crystallization phase boundaries, including the scaling behavior. In addition, we present analytic approximations that capture the asymptotic behavior of the boundaries and provide insight into their scaling.

Our experimental system consists of sterically stabilized polymethylmethacrylate (PMMA) colloidal spheres labeled with nitro-2-1,3-benzoxadiazol-4-yl (NBD) dye and suspended in a solvent mixture of decahydronapthalene (dielectric constant $\epsilon = 2.1$, $\rho = 0.881$ g/mL, $n = 1.48$) and tetrachloroethylene ($\epsilon = 2.5$, $\rho = 1.623$ g/mL, $n = 1.51$) in a mass ratio of 1:1.1. We load suspensions into rectangular glass capillaries (Vitrocom) with inner dimensions $0.1 \times 2 \times 50$ mm. The particles and solvent have sufficiently similar ρ that we do not observe sedimentation for the duration of the experiment, and have sufficiently closely matched n that we can visualize all particles individually in 3D using a laser-scanning confocal fluorescence microscope (Leica TCS SP5) [29].

We solubilize charge using aerosol-OT (sodium di-2-ethylhexylsulfosuccinate, or AOT), which, above its critical micelle concentration, forms reverse micelles whose size does not depend on AOT concentration C_{AOT} [30–32]. Neutral reverse micelles can interact reversibly via a symmetric two-body mechanism to yield two reverse micelles with opposite charges [28,33]; the fraction of ionized reverse micelles χ is about 10^{-5}, independent of C_{AOT}. To quantify the effects of the reverse micelles on screening of charges,

---

[*] Corresponding author: plu@fas.harvard.edu

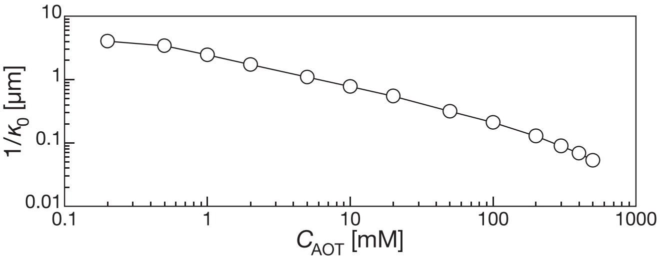

FIG. 1. $1/\kappa_0$ as a function of C_{AOT}, determined from conductivity and viscosity measurements.

we formulate reverse-micelle suspensions with a range of C_{AOT}; at each concentration, we measure the conductivity σ with an immersion probe (Scientifica), and viscosity η with a glass viscometer (Cannon). From these data, we determine the screening length, $1/\kappa_0 \equiv 1/\sqrt{4\pi\lambda_B n_{\mathrm{ion}}}$, where the Bjerrum length λ_B is 24 nm in a solvent with $\epsilon = 2.3$; the total number density of equally sized monovalent ions is $n_{\mathrm{ion}} \equiv 6\pi\eta a_{\mathrm{h}}\sigma/e^2$, where e is the elementary charge and a_h is the hydrodynamic radius. We find that the screening length $1/\kappa_0$ decreases monotonically with C_{AOT} [30], as shown in Fig. 1.

To explore the phases that form in these mixtures, we formulate suspensions of the colloidal particles with radius $a = 0.70$ μm at $\phi = 0.23$, and vary C_{AOT} over a wide range. We collect three-dimensional (3D) image stacks of these suspensions with a confocal microscope, and use software to locate the 3D position of each particle [34–36]. To ensure good statistics, we calculate the 3D pair correlation function, $g(r)$, from at least several thousand particles in each sample. When $C_{\mathrm{AOT}} = 0$, the particles are essentially uncharged, and their behavior is well-described as that of a hard sphere fluid; as C_{AOT} increases, the particles become increasingly charged leading to correlations between particle positions. For $C_{\mathrm{AOT}} = 1$ mM, we observe a strongly correlated liquid, shown in the 2D confocal image in Fig. 2(a), collected several particle layers from the coverslip, and as with all collected images is representative of the structure throughout the depth of the sample; $g(r)$ for this sample has broad, low peaks, as shown with the dotted purple curve in Fig. 2(e). Upon further increasing C_{AOT}, the particles undergo a crystallization transition; at $C_{\mathrm{AOT}} = 5$ mM, we observe a disorder-order transition from the fluid to a bcc Wigner crystal, as shown in Fig. 2(b); strikingly, while the particles remain well separated due to their charge, the order and quality of the bcc crystal lattice is sufficiently high that we can locate and index many of the major peaks in $g(r)$ from the known structure, as shown in Fig. 2(f). Further increasing C_{AOT}, we observe a solid-solid crystal phase transition from bcc to fcc structures, shown in Fig. 2(c), and again we can index many of the main $g(r)$ peaks, as shown in Fig. 2(g). Remarkably, however, when C_{AOT} exceeds 200 mM, we observe reentrant melting: the fcc crystal is fluidized, with no crystalline peaks present in $g(r)$, as shown with the blue curve in Fig. 2(e).

To explore more fully the phase behavior of these particles, we repeat the above experiments at several ϕ. The general phase behavior with increasing reverse-micelle concentration, changing from a fluid to bcc to fcc and ultimately to a re-entrant fluid, persists over a wide range of ϕ well below the hard-sphere crystal boundary, and for several particle sizes $a = 0.46$, 0.70, and 0.96 μm, as shown with symbols in the phase diagrams in Figs. 3(a)–3(c). For sufficiently low $\phi \leqslant 0.05$, the system remains fluid and does not crystallize anywhere, as shown in the figure. For samples that crystallize at $\phi \approx 0.1$, only the bcc crystal phase is observed; only above $\phi \approx 0.2$ do we observe a clear bcc-fcc phase boundary, which occurs at lower C_{AOT} for increasing ϕ. By contrast, the reentrant fcc-fluid boundary occurs at higher C_{AOT} as ϕ increases. The qualitative behavior, with the fcc and bcc crystal phases and the reentrant melting, remains the same for all a, as shown with symbols in Figs. 3(a)–3(c).

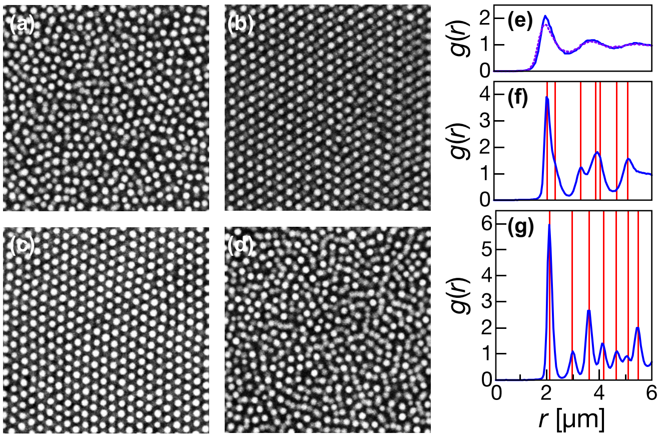

FIG. 2. (Color online) Confocal microscopy images of PMMA particles at $\phi = 0.23$ and (a) $C_{\mathrm{AOT}} = 1$ mM, fluid; (b) $C_{\mathrm{AOT}} = 5$ mM, bcc crystal; (c) $C_{\mathrm{AOT}} = 50$ mM, fcc crystal; (d) $C_{\mathrm{AOT}} = 200$ mM, fluid. (e) $g(r)$ for fluid samples in (a) and (d) shown with dotted purple and solid blue curves, respectively. (f) $g(r)$ for bcc crystal in (b), with major peaks (red lines) corresponding to indices (left to right) $\{\frac{2}{3}\frac{2}{3}\frac{2}{3}\}$, $\{100\}$, $\{\frac{1}{2}\frac{1}{2}0\}$, $\{\frac{6}{11}\frac{2}{11}\frac{2}{11}\}$, $\{\frac{1}{3}\frac{1}{3}\frac{1}{3}\}$, $\{\frac{1}{2}00\}$, and $\{\frac{6}{19}\frac{6}{19}\frac{2}{19}\}$. (g) $g(r)$ for fcc crystal in (c), with peaks corresponding to $\{110\}$, $\{100\}$, $\{\frac{2}{3}\frac{1}{3}\frac{1}{3}\}$, $\{\frac{1}{2}\frac{1}{2}0\}$, $\{\frac{3}{5}\frac{1}{5}0\}$, $\{\frac{1}{3}\frac{1}{3}\frac{1}{3}\}$, and $\{\frac{3}{7}\frac{2}{7}\frac{1}{7}\}$.

To explain this behavior, we construct a model that accounts for the basic physical interactions among the micelles and particles at a microscopic level. AOT reverse micelles affect the particle surface charge through two coupled equilibria. The first reaction is the self-ionization equilibrium of reverse-micelle pairs, described by $2Mic \rightleftharpoons Mic^- + Mic^+$, where Mic refers to a neutral reverse micelle [28]. We characterize this reaction with the constant K_{M}, which we use as a fitting parameter. In the bulk, the total ion concentration is $n_{\mathrm{ion}} = [Mic^+] + [Mic^-] = 2\sqrt{K_{\mathrm{M}}}[Mic]$. The second reaction is the charging of the colloidal surface through charge exchange of a neutral reverse micelle Mic and a neutral surface site S to form a cationic reverse micelle Mic^+ and negative surface site S^-: $S + Mic \rightleftharpoons S^- + Mic^+$ [30], characterized by the equilibrium constant K_{C}. We assume that the cationic reverse-micelle concentration in the vicinity of the colloid surface, where $r = a$, follows the Boltzmann distribution $[Mic^+]_0 = \frac{1}{2}n_{\mathrm{ion}}\exp[-\beta e\psi(r = a)]$ where $\psi(r)$ is the unknown electrostatic potential. We represent the small fraction of charged surface groups f

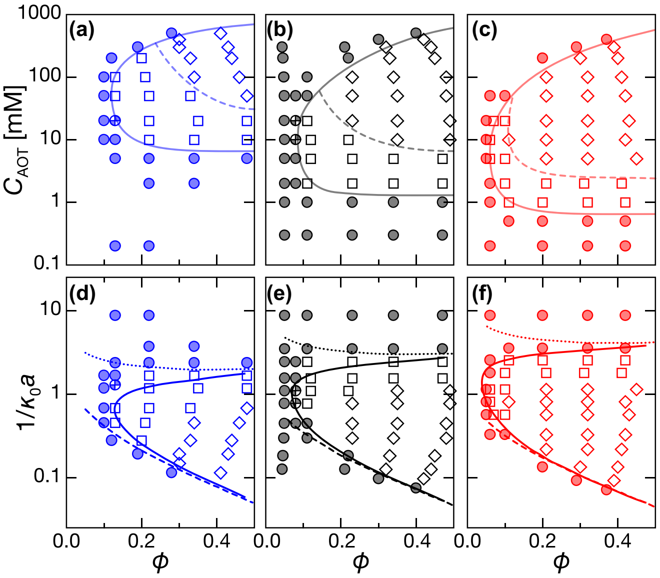

FIG. 3. (Color online) Phase diagrams for charged crystallization and reentrance as a function of ϕ and C_{AOT} for particles with (a) $a = 0.46$ μm (blue), (b) 0.70 μm (black), and (c) 0.96 μm (red). Experimentally determined phases marked with symbols: filled circles (fluid), open squares (bcc), open diamonds (fcc), and semifilled symbols (fluid-bcc coexistence). Solid curves denote experimental fluid-crystal boundary; solid-solid transition between bcc and fcc marked with dashed curves. (d)–(f) Phase diagrams of the same samples as a function of ϕ and $1/\kappa_0 a$, using the mapping from C_{AOT} to $1/\kappa_0$ in Fig. 1. Solid curves indicate numerical predictions, which closely follow the experimental data. Analytic predictions for the phase boundaries at low and high C_{AOT} are marked with dotted and dashed lines, respectively.

as

$$f \equiv \frac{[S^-]}{[S]} = \frac{K_{\mathrm{C}}[Mic]}{[Mic^+]_0} = \frac{K_{\mathrm{C}} \exp[\beta e \psi(r = a)]}{\sqrt{K_{\mathrm{M}}}}. \tag{1}$$

The total colloidal charge is $Ze = -4\pi a^2 m f e$, where m is the areal density of chargeable surface groups.

To compute Z and $\psi(r = a)$ self-consistently, we calculate the full electrostatic potential $\psi(r)$ in a charge-neutral, spherical Wigner-Seitz cell [37–39] with radius $R = a\phi^{-1/3}$, containing a spherical colloidal particle centered at the origin. On the colloid surface we impose Gauss's law, $\beta e \frac{\partial \psi(r)}{\partial r}|_{r=a} = -Z\lambda_{\mathrm{B}}/a^2$. For $a < r < R$ the ionic reverse-micelle concentrations follow Boltzmann distributions $\frac{1}{2} n_{\mathrm{ion}} \exp[\pm \beta e \psi(r)]$; we therefore solve numerically the Poisson-Boltzmann (PB) equation of the form

$$\begin{aligned} \beta e \frac{\partial^2 \psi(r)}{\partial r^2} + \beta e \frac{2}{r} \frac{\partial \psi(r)}{\partial r} &= \kappa_0^2 \sinh[\beta e \psi(r)], \\ \left.\frac{\partial \psi(r)}{\partial r}\right|_{r=R} &= 0, \\ \left.\beta e \frac{\partial \psi(r)}{\partial r}\right|_{r=a} &= 4\pi \lambda_{\mathrm{B}} \left(\frac{m K_{\mathrm{C}}}{\sqrt{K_{\mathrm{M}}}} \right) \\ &\quad \times \exp[\beta e \psi(r = a)] \end{aligned} \tag{2}$$

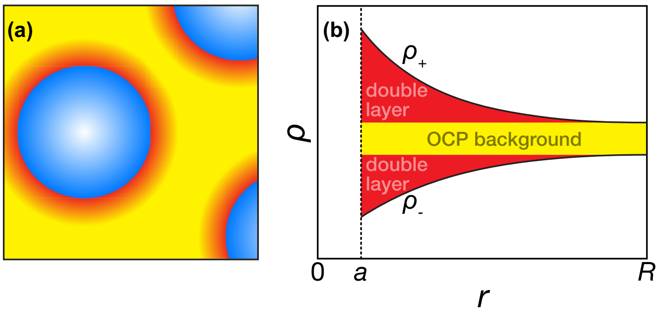

FIG. 4. (Color online) (a) Illustration of charged particles (blue), their double layers (red), and the OCP background (yellow). (b) Typical ion concentration profiles $\rho_\pm(r)$ around a negatively charged colloidal sphere of radius a in a cell of radius R in the weak-screening regime $\kappa_0 R \lesssim 1$, such that the OCP-like ionic background charge $\rho_+(R) - \rho_-(R) = \rho_{\mathrm{bg}}$ (see text) is nonvanishing. By charge neutrality the effective colloidal charge equals $(4\pi/3)(R^3 - a^3)\rho_{\mathrm{bg}}$, and the corresponding OCP point charge is $Z_{\mathrm{OCP}} = (4\pi/3)R^3\rho_{\mathrm{bg}}$.

for given λ_{B}, a, ϕ, and κ_0, and for fixed combinations of $mK_{\mathrm{C}}/\sqrt{K_{\mathrm{M}}}$, which we fit as a single parameter. The calculation yields not only Ze and $\psi(r = a)$, but also the Donnan potential $\psi(r = R)$ and the far-field background ionic charge $\rho_{\mathrm{bg}} = -n_{\mathrm{ion}} \sinh[\beta e \psi(r = R)]$.

To determine where the system crystallizes, we map the colloidal dispersions onto a one-component plasma (OCP) of point particles of density $n \equiv 3\phi/4\pi a^3$ and charge $Z_{\mathrm{OCP}} \equiv -\rho_{\mathrm{bg}}/n$, to satisfy global OCP neutrality, with a uniform background charge ρ_{bg}, as illustrated in Fig. 4. The OCP crystallizes if $\Gamma > 106$ [40,41] (see Appendix), where the OCP coupling parameter is defined as $\Gamma \equiv Z_{\mathrm{OCP}}^2 \lambda_{\mathrm{B}} n^{1/3}$; this threshold yields a simple new freezing criterion that takes the standard PB cell-model calculations as input. Therefore, to calculate the phase boundaries for comparison with the experimental data, we solve numerically for $\Gamma = 106$ using ρ_{bg}, as obtained from the numerical solution of Eq. (2), fitting only the single parameter $mK_{\mathrm{C}}/\sqrt{K_{\mathrm{M}}} = 5.0 \times 10^2 \mu\mathrm{m}^{-2}$.

To facilitate comparison between samples, and with theory, we convert the micellar concentration to the dimensionless product $1/\kappa_0 a$, determined by mapping the experimental C_{AOT} to $1/\kappa_0$ via the empirical data in Fig. 1; the experimental data are shown with the symbols in Figs. 3(d)–3(f). This representation allows a direct comparison between the experimentally observed phase boundaries, and those predicted by our model. Strikingly, the theoretical predictions are in excellent quantitative agreement with experimental phase boundaries for all a, as shown by the solid curves in Figs. 3(d)–3(f). Our new crystallization criterion might be expected to apply only in the low-AOT limit $1/\kappa_0 a > 1$, where the dispersion is OCP-like; however, we observe similar accuracy with the well-established empirical criteria [42–44] for point-Yukawa fluids even for $1/\kappa_0 a < 0.1$. Moreover, our predictions are accurate even at high ϕ; our criterion accounts for the significant hard-core exclusion effects that the ions experience, even as Coulombic repulsion keeps particles well separated.

The quantitative success of our numerical model suggests that a more analytic approach might also predict accurately the onset of crystallization, in the weak- and strong-screening regimes. For low C_{AOT}, the concentration of co-ions is negligible, while the counterions form a uniform background, such that $\rho_{\mathrm{bg}} \approx [Mic^+]_0$. Following the described charging equilibrium $Z = -(\kappa_0 a)^2 m K_{\mathrm{C}}/(2\sqrt{K_{\mathrm{M}}}\lambda_{\mathrm{B}}[Mic^+]_0)$ and substituting $Z_{\mathrm{OCP}} = Z/(1-\phi)$ in this limit, we obtain the analytic expression

$$\Gamma \approx (4\pi/3)^{2/3}\phi^{-2/3}(1-\phi)^{-1}(\kappa_0 a^2)^2 m K_{\mathrm{C}}/2\sqrt{K_{\mathrm{M}}}. \qquad (3)$$

We calculate the phase boundary by determining ϕ and κ_0 where $\Gamma = 106$; remarkably, this yields a predicted phase boundary which converges closely to the numerical calculation and experimental boundary at high ϕ, as shown with the dotted lines in Figs. 3(d)–3(f).

In the concentrated AOT regime, where $1/\kappa_0 a \ll 1$, we assume a small $\psi(r)$ throughout the cell, due to efficient ionic screening. We therefore utilize linear screening theory to find that the general solution to the potential profile is of the form $\psi(r) = A\exp(\kappa_0 r)/r + B\exp(-\kappa_0 r)/r$. We calculate the constants A and B by using cell neutrality and approximate the surface potential to be moderate, $\beta e\psi(a) \approx 1$. The background charge is $\rho_{\mathrm{bg}} = -n_{\mathrm{ion}}\beta e\psi(R)$. We substitute these into the expression for Z_{OCP}, and again use the criterion $\Gamma = 106$ to yield analytical predictions for the reentrant boundaries. Strikingly, our simple model predicts reentrance in close quantitative agreement with both the numerical calculations and the experimental data over the entire range ϕ, as marked with the dashed lines in Figs. 3(d)–3(f).

Interestingly, the phase boundaries for different a occur at different ϕ and $1/\kappa_0 a$; there is no universal behavior of the data in this dimensionless representation, indicating that particle size plays a nontrivial role. From Eq. (3), at low C_{AOT}, Γ depends only on $\kappa_0 a^2$ and ϕ; the ϕ dependence is weak, featuring a shallow minimum at $\phi = 0.4$, but is roughly constant, consistent with the nearly constant C_{AOT} observed for this boundary in the experimental data. By contrast, at high C_{AOT} and close to the phase boundary, Γ shows very little remaining dependence on a, when expressed as a function of $\kappa_0 a^2$, ϕa, and a. These mathematical properties suggest that the systems with different a may behave in the same way, when their phases are plotted as functions of the *dimensional* parameters $1/(\kappa_0 a^2)$ and ϕa.

To test this, we replot all the experimental data, as functions of $1/(\kappa_0 a^2)$ and ϕa; remarkably, all of the experimental data from all three a collapse onto a universal phase diagram, with the same onset of crystallization and reentrance for all samples, shown with symbols in Fig. 5. Our theoretical model predicts this boundary, as shown by the overlapping solid curves in Fig. 5. That the collapse occurs when the data are plotted as a function of parameters that explicitly include a length scale, as opposed to the dimensionless case, is particularly striking; moreover, our numerical calculations suggest that this nondimensionless scaling should apply over a larger range of a, extending over half an order of magnitude beyond the particle sizes used in these experiments. However, the origin of this dimensional data collapse remains an open question.

The excellent agreement between the assumptions of our theoretical model and our experimental data suggests that the same mechanism may drive electrostatically induced phase transitions in general. Although crystallization curves are fitted accurately, the observed bcc-fcc transition curves cannot be reproduced within our approach, as the OCP does not show fcc ordering. Nevertheless, our model can now be used to predict a wide range of behaviors in charged particle systems, and the flexibility and extended length scales possible through the use of nonpolar solvents make these an attractive model system for the study of other phase behavior.

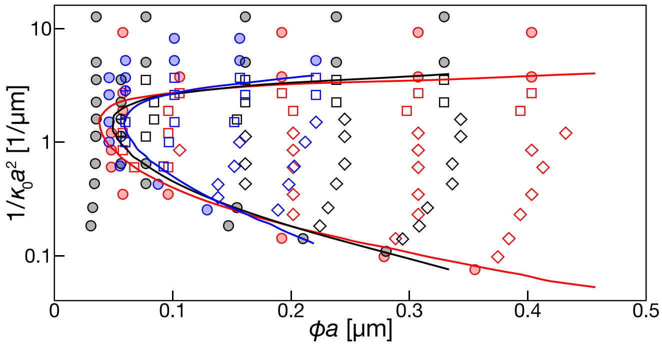

FIG. 5. (Color online) Phase diagram for all particle radii, with $a = 0.46$ μm (blue), 0.70 μm (black), and 0.96 μm (red), with experimental data and numerical calculations as in Fig. 2, shown as functions of dimensional parameters ϕa and $1/(\kappa_0 a^2)$. All experimental data collapse onto a single behavior (symbols), which is closely modeled by theoretical predictions (curves). Symbols are as in Fig. 3.

T.K., N.B., and P.J.L. contributed equally to this work. This work was supported by NASA (NNX13AQ48G), the NSF (DMR-1310266 and DMR-1206765), the Harvard Materials Research Science and Engineering Center (DMR-1420570), and JSPS Postdoctoral Fellowships for Research Abroad, and is part of the D-ITP consortium, a program of the Netherlands Organisation for Scientific Research (NWO) that is funded by the Dutch Ministry of Education, Culture and Science (OCW).

APPENDIX

The Coulomb coupling parameter Γ plays a pivotal role in the characterization of OCPs, and is defined as the Coulomb interaction energy expressed in units of the thermal energy kT for two particles at a typical interparticle distance D: $\Gamma \equiv Z^2\lambda_{\mathrm{B}}/D$, where Z is the particle charge. Here we define $D \equiv n^{-1/3}$, where n is the particle density, consistent with recent studies [42]. However, other pioneering studies on OCP freezing [40,41] use a slightly different definition of the interparticle distance, $D^* \equiv (4\pi n/3)^{-1/3}$; this results in a small change to the coupling parameter definition: $\Gamma^* \equiv Z^2\lambda_{\mathrm{B}}/D^* \approx 1.61\Gamma$. These studies show that a Coulomb lattice is the most favourable configuration when the coupling parameter exceeds a critical value, $\Gamma^* \simeq 171$ [41]. Consequently, in our study, the phase transition between the fluid and crystal should occur very close to $\Gamma = 106$; we use this criterion to construct our phase diagrams.

[1] U. Gasser, E. R. Weeks, A. Schofield, P. N. Pusey, and D. A. Weitz, Science **292**, 258 (2001).
[2] A. Yethiraj and A. van Blaaderen, Nature (London) **421**, 513 (2003).
[3] P. Schall, I. Cohen, D. A. Weitz, and F. Spaepen, Science **305**, 1944 (2004).
[4] P. Schall, I. Cohen, D. A. Weitz, and F. Spaepen, Nature (London) **440**, 319 (2005).
[5] A. Kose and S. Hachisu, J. Colloid Interface Sci. **46**, 460 (1974).
[6] B. J. Alder, W. G. Hoover, and D. A. Young, J. Chem. Phys. **49**, 3688 (1968).
[7] P. N. Pusey and W. van Megen, Nature (London) **320**, 340 (1986).
[8] W. K. Kegel and A. van Blaaderen, Science **287**, 290 (2000).
[9] J. L. Harland and W. van Megen, Phys. Rev. E **55**, 3054 (1997).
[10] S. Hachisu, Y. Kobayashi, and A. Kose, J. Colloid Interface Sci. **42**, 342 (1973).
[11] A. Kose, M. Ozaki, K. Takano, Y. Kobayashi, and S. Hachisu, J. Colloid Interface Sci. **44**, 330 (1973).
[12] S. Hachisu and Y. Kobayashi, J. Colloid Interface Sci. **46**, 470 (1974).
[13] B. J. Ackerson and N. A. Clark, Phys. Rev. Lett. **46**, 123 (1981).
[14] P. Pieranski, Contemp. Phys. **24**, 25 (1983).
[15] D. Hone, S. Alexander, P. M. Chaikin, and P. Pincus, J. Chem. Phys. **79**, 1474 (1983).
[16] K. Kremer, M. O. Robbins, and G. S. Grest, Phys. Rev. Lett. **57**, 2694 (1986).
[17] W. Y. Shih, I. A. Aksay, and R. Kikuchi, J. Chem. Phys. **86**, 5127 (1987).
[18] M. O. Robbins, K. Kremer, and G. S. Grest, J. Chem. Phys. **88**, 3286 (1988).
[19] K. Ito, K. Sumaru, and N. Ise, Phys. Rev. B **46**, 3105 (1992).
[20] H. Fudouzi and Y. Xia, Adv. Mater. **15**, 892 (2003).
[21] C. P. Royall, M. E. Leunissen, A.-P. Hynninen, M. Dijkstra, and A. van Blaaderen, J. Chem. Phys. **124**, 244706 (2006).
[22] T. Kanai, T. Sawada, A. Toyotama, and K. Kitamura, Adv. Funct. Mater. **15**, 25 (2005).
[23] E. B. Sirota, H. D. Ou-Yang, S. K. Sinha, P. M. Chaikin, J. D. Axe, and Y. Fujii, Phys. Rev. Lett. **62**, 1524 (1989).
[24] R. Williams and R. Crandall, Phys. Lett. A **48**, 225 (1974).
[25] P. Chaikin, P. Pincus, S. Alexander, and D. Hone, J. Colloid Interface Sci. **89**, 555 (1982).
[26] M. E. Leunissen, C. G. Christova, A.-P. Hynninen, C. P. Royall, A. I. Campbell, A. Imhof, M. Dijkstra, R. van Roij, and A. van Blaaderen, Nature (London) **437**, 235 (2005).
[27] G. N. Smith, S. Alexander, P. Brown, D. A. J. Gillespie, I. Grillo, R. K. Heenan, C. James, R. Kemp, S. E. Rogers, and J. Eastoe, Langmuir **30**, 3422 (2014).
[28] R. Kemp, R. Sanchez, K. J. Mutch, and P. Bartlett, Langmuir **26**, 6967 (2010).
[29] P. J. Lu, E. Zaccarelli, F. Ciulla, A. B. Schofield, F. Sciortino, and D. A. Weitz, Nature (London) **453**, 499 (2008).
[30] M. F. Hsu, E. R. Dufresne, and D. A. Weitz, Langmuir **21**, 4881 (2005).
[31] K. Mukherjee, S. P. Moulik, and D. C. Mukherjee, Langmuir **9**, 1727 (1993).
[32] M. B. Mathews and E. Hirschhorn, J. Colloid Sci. **8**, 86 (1953).
[33] I. D. Morrison, Colloids Surf. A **71**, 1 (1993).
[34] P. J. Lu, P. A. Sims, H. Oki, J. B. Macarthur, and D. A. Weitz, Opt. Express **15**, 8702 (2007).
[35] P. J. Lu, J. C. Conrad, H. M. Wyss, A. B. Schofield, and D. A. Weitz, Phys. Rev. Lett. **96**, 028306 (2006).
[36] P. J. Lu, M. Shutman, E. Sloutskin, and A. V. Butenko, Opt. Express **21**, 30755 (2013).
[37] S. Alexander, P. M. Chaikin, P. Grant, G. J. Morales, P. Pincus, and D. Hone, J. Chem. Phys. **80**, 5776 (1984).
[38] E. Trizac, L. Bocquet, M. Aubouy, and H. H. von Grünberg, Langmuir **19**, 4027 (2003).
[39] F. Smallenburg, N. Boon, M. Kater, M. Dijkstra, and R. van Roij, J. Chem. Phys. **134**, 074505 (2011).
[40] W. L. Slattery, G. D. Doolen, and H. E. DeWitt, Phys. Rev. A **21**, 2087 (1980).
[41] S. Ichimaru, Rev. Mod. Phys. **54**, 1017 (1982).
[42] O. Vaulina and S. Khrapak, J. Exp. Theor. Phys. **90**, 287 (2000).
[43] S. Hamaguchi, R. T. Farouki, and D. H. E. Dubin, Phys. Rev. E **56**, 4671 (1997).
[44] A.-P. Hynninen and M. Dijkstra, Phys. Rev. E **68**, 021407 (2003).